SCIENTIFIC REPORTS
nature research

Check for updates

OPEN

Viscoelasticity in simple indentation-cycle experiments: a computational study

Yu. M. Efremov[1]✉, S. L. Kotova[1,2] & P. S. Timashev[1,2,3,4]

Instrumented indentation has become an indispensable tool for quantitative analysis of the mechanical properties of soft polymers and biological samples at different length scales. These types of samples are known for their prominent viscoelastic behavior, and attempts to calculate such properties from the indentation data are constantly made. The simplest indentation experiment presents a cycle of approach (deepening into the sample) and retraction of the indenter, with the output of the force and indentation depth as functions of time and a force versus indentation dependency (force curve). The linear viscoelastic theory based on the elastic–viscoelastic correspondence principle might predict the shape of force curves based on the experimental conditions and underlying relaxation function of the sample. Here, we conducted a computational analysis based on this theory and studied how the force curves were affected by the indenter geometry, type of indentation (triangular or sinusoidal ramp), and the relaxation functions. The relaxation functions of both traditional and fractional viscoelastic models were considered. The curves obtained from the analytical solutions, numerical algorithm and finite element simulations matched each other well. Common trends for the curve-related parameters (apparent Young's modulus, normalized hysteresis area, and curve exponent) were revealed. Importantly, the apparent Young's modulus, obtained by fitting the approach curve to the elastic model, demonstrated a direct relation to the relaxation function for all the tested cases. The study will help researchers to verify which model is more appropriate for the sample description without extensive calculations from the basic curve parameters and their dependency on the indentation rate.

Micro- and nanoindentation (including atomic force microscopy, AFM) have become indispensable tools for the quantitative analysis of the mechanical properties of soft polymers and biological samples with the focus on the corresponding micro- and nanoscale[1–3]. Their benefits include a small sample size and simple preparation, an easily achievable environmental control (e.g. a temperature-controlled fluid cell), a possibility of region-specific mapping and coupling with optical techniques. The purpose of the indentation analysis is to link the indentation data to the meaningful mechanical properties of the sample. Biological samples generally possess time-dependent viscoelastic properties, which can be observed at both the tissue and cellular levels. The important role of viscoelastic properties, as opposed to a purely elastic behavior, has been shown in the studies of different cell phenomena including cancer[4,5], contractile prestress[6], and response to the substrate stiffness[7]. Mathematical models are used to describe the viscoelastic behavior in terms of the relaxation functions. A set of traditional and fractional linear viscoelasticity models are used to describe the sample properties and facilitate the comparison of the parameters across different studies[8–10].

Recently, a large variety of indentation-based methods have been developed to measure and map viscoelastic properties[6,11–15]. Most of them are using modifications of the testing protocol by including constant stress or constant strain phases and oscillatory indentation. However, there are also methods to extract viscoelastic properties directly from the simplest indentation experiment presenting a cycle of approach (deepening into the sample) and retraction of the indenter[5,16–18]. Indentation of a viscoelastic body presents a complex problem

[1]Institute for Regenerative Medicine, Sechenov University, 8 Trubetskaya St., Moscow 119991, Russia. [2]N.N. Semenov Institute of Chemical Physics, 4 Kosygin St., Moscow 119991, Russia. [3]Institute of Photon Technologies of Federal Scientific Research Centre "Crystallography and Photonics" of Russian Academy of Sciences, Pionerskaya 2, Troitsk, Moscow 108840, Russia. [4]Chemistry Department, Lomonosov Moscow State University, Leninskiye Gory 1-3, Moscow 119991, Russia. ✉email: yu.efremov@gmail.com

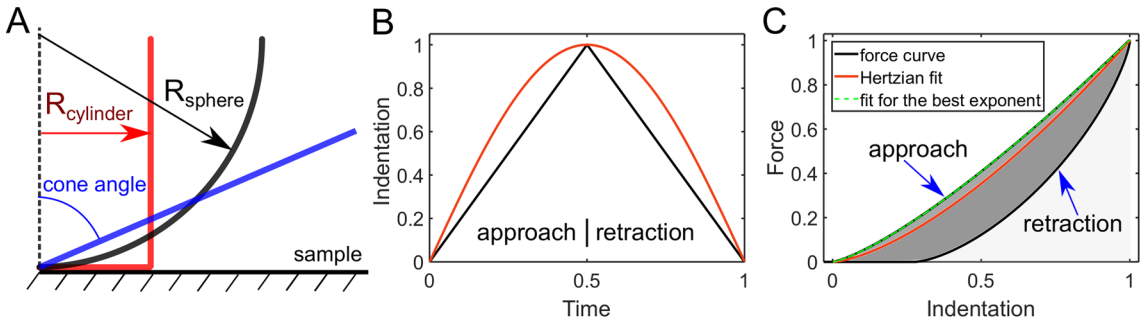

Figure 1. (**A**) The used indenter (probe) geometries: flat-ended cylinder, sphere, and cone. (**B**) The applied indentation histories, triangular (black) and sinusoidal (red) ramps. (**C**) The parameters, extracted for the force curves: apparent Young's modulus (YM), obtained from the Hertzian fit (red curve); the approach curve exponent, obtained from the fit with an exponent as a fitting parameter; the normalized hysteresis area (NHA), obtained as the area enclosed in the force curve (dark-grey area) divided by the area under the approach curve (light-grey plus dark-grey area). Here, the case of the spherical probe and the springpot viscoelastic model is shown as an example.

with time-varying boundary conditions. The correspondence principle that is used for the problems involving a linear, isotropic viscoelastic body breaks down for the complex indenter shapes and indentation conditions. Lee and Radok obtained an expression for the indentation force and spherical indentation by replacing the elastic modulus in the Hertz solution[19,20] by hereditary integral involving the relaxation response function[21]. However, this solution was found to be invalid when the contact radius decreases with time; the issue was addressed later by Hunter[22], Graham[23] and Ting[24,25]. In any case, the viscoelastic analysis of indentation experiments is much more computationally sophisticated than the analysis based on simple elastic assumptions, and thus, the latter is prevailing in the experimental studies. Moreover, a thorough analysis of force-indentation curves predicted by different viscoelastic models has not been performed before.

This work aims at finding how the viscoelastic relaxation function affects the shape of force curves obtained at different indentation conditions. We analyzed how some basic characteristic curve features change when acquisition parameters such as the indentation rate or indenter shape are varied. These basic features (apparent Young's modulus, normalized hysteresis area, the curve exponent) can be routinely obtained from experimental curves. Three approaches were used to obtain force curves here: an analytical solution, for the cases where the closed-form analytical solution might be obtained, a numerical solution based on the direct calculation of the Ting's equations[5], and a FEM simulation-based solution. We performed the analysis for three types of indenter geometries (cylinder, cone, sphere), two types of indentation histories (triangular and sinusoidal ramps), and several types of traditional and fractional viscoelastic models.

Results

The main purpose of the study is to find how the viscoelastic relaxation function of a sample will be reflected in the shape of force curves obtained by indentation. Especially, we are interested in some characteristic features and how they might change when the acquisition parameters such as the indentation rate (inverse of indentation time) are varied. The force curves were obtained using three approaches: an analytical solution, for the cases where the closed-form analytical solution might be obtained, a numerical solution based on the direct calculation of the Ting's equations, and a FEM simulation solution. The latter one is also a numerical solution by nature, but here we will call it a "simulation solution" to distinguish from the former one. We performed such analysis for three types of indenter geometries (cylinder, cone, sphere), two types of indentation histories (triangular and sinusoidal ramps), and several types of viscoelastic models (Fig. 1).

For all the scenarios (a combination of the probe geometry, indentation history, and viscoelastic model) that provided the closed-form analytical solution, we found a perfect agreement between the analytical and numerical solutions (Figs. S1, S2). This confirms that the numerical solution could effectively substitute the analytical one, and it is especially useful for the cases where the analytical solution could not be obtained. These cases include both complex indentation histories (e.g. non-linear indentation due to a cantilever deflection during the piezo movement, non-linearity in the piezo movement itself) and viscoelastic models (with a large number of elementary elements). The available analytical solutions are presented in Appendix A.

The FEM analysis was performed on two selected sets of parameters for each viscoelastic model, probe geometry and indentation history (total of 24 simulations). The FEM simulation solutions were close to the analytical (where they were obtained) and numerical solutions for all the selected model parameters (Figs. S1, S2). Some observed differences could originate from the finite-size effects. However, the FEM solution is much more time-consuming in comparison with the numerical solution used here.

Therefore, to facilitate the analysis of the force curves, we used only the numerical solutions in the consequent study. Several considerations were taken into account to optimize the analysis:

1. The geometrical parameters of the probe (e.g. cylinder radius, cone angle) will not affect the shape of the curve after the normalization, thus they were not varied. They were arbitrarily set to 5 μm (sphere radius), 0.4 μm (cylinder radius), 85° (half-angle of the cone).

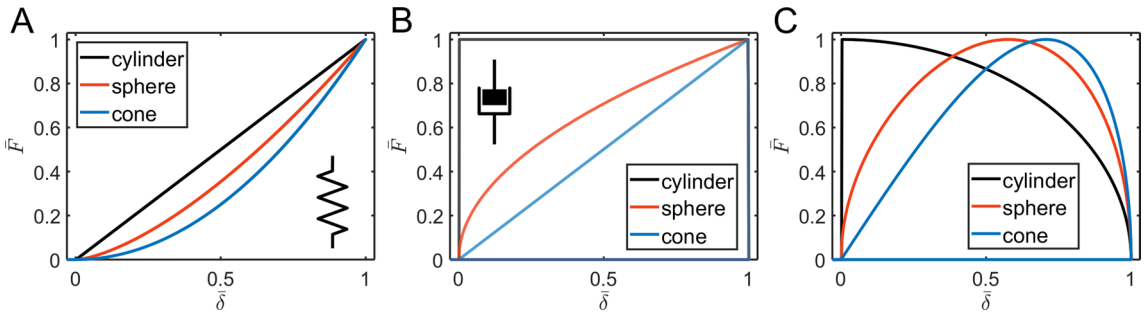

Figure 2. The force versus indentation curves in the normalized coordinates for the spring (**A**) and dashpot (**B**,**C**) elements. The spring element provides the curves described by the Hertzian mechanics, with the curve exponent defined by the probe geometry and zero hysteresis. In contrast, the dashpot provides complete curves with complete hysteresis (zero force during the retraction) that depend on the indentation history, triangular (**B**) or sinusoidal (**C**) ramp.

2. The indentation depth does not affect the shape of the curve since the materials are assumed to behave within the limits of the linear viscoelasticity. Therefore, the change in the indentation depth equals to the change in the indentation speed in the normalized coordinates ($\bar{\delta}(t) = \bar{\delta}(t)/\delta_{\max}, \bar{F}(\delta(t)) = F(\delta(t))/F_{\max}$). The results are presented in the normalized coordinates or in the actual coordinates (the maximum indentation depth was arbitrarily set to 100 nm, the units of nm for the distance and nN for the force are used in the figures) for a better representation. Exact values of some viscoelastic model parameters do not affect the shape of the curves in the normalized coordinates, while the relations between the parameters do affect the shape of the curves and define the characteristic times of the model.
3. The following parameters were extracted from the force curves. The normalized hysteresis area (NHA), defined as the area enclosed between the approach and retraction curves divided by the area under the approach curve (Fig. 1C). This parameter represents the energy dissipation during the indentation cycle, and thus it is especially useful. The NHA may have values in the range between zero (elastic behavior, the approach and retraction curves are coinciding with each other) and one (all the energy is dissipating); in the intermittent regime, the approach curve is always laying above the retraction curve. The second parameter is the power-law exponent of the simple power-law fit applied to the approach curve. Basically, it represents how far the curve deviates from the Hertzian fit. Additionally, the apparent Young's modulus (YM) extracted from the Hertzian fit of the complete curve (with the fixed exponent value corresponding to the probe geometry) was extracted and its dependency from the indentation time was studied. The graphs are shown in the coordinates of the indentation time t_{ind}, defined as the total time of indentation cycle, and the corresponding indentation rate is the inverse value of the indentation time.

Simplest spring-dashpot combinations. We begin the analysis with the simplest analytic viscoelastic constitutive models which present a single spring or a dashpot element and their combinations. A spring element symbolizes an ideal elastic behavior; the stress is linearly proportional to the strain: $\sigma(t) = k\varepsilon(t)$. For this element, the relaxation function is constant in time ($E(t) = E$), and the Ting's equation solution corresponds to the well-known Hertzian solution of the form:

$$F(\delta(t)) = C_{geom} E \delta^n. \tag{1}$$

The $n = 1, 1.5, 2$ for the cylindrical, spherical and conical probe respectively, the geometrical coefficients are: $C_{cylinder} = 2R, C_{sphere} = 4\sqrt{R}/3, C_{cone} = 2(tan\alpha_{cone})/\pi$. The numerical algorithm and FEM simulations provide the force-indentation curves which are analogous to the analytical solution. The force curves show a zero hysteresis area (NHA = 0), the curve exponents match with the predicted ones (Fig. 2A).

For a dashpot element, the stress is proportional to the strain rate by Trouton's (or Newton's) law: $\sigma(t) = \eta d\varepsilon(t)/dt$ (η is the viscoelastic coefficient or viscosity with the units of [Pa s], where symbol s is used for seconds) according to the behavior of an ideal Newton liquid. The relaxation function is $E(t) = \eta\delta_D(t)$, where $\delta_D(t)$ is the Dirac delta function. This viscosity is mostly related to the compressive viscoelastic coefficient (also known as the Trouton coefficient) because indentation measurements involve application of compressive forces normal to the sample surface[26]. The analytical solution (eq. A3 in the Appendix) shows that the force drops to zero then the cantilever goes up (retracts), as expected for the viscous material. Thus, the NHA is always equal to one (all energy is dissipated). The shape of the curve is very different from the Hertzian shape and shows a power-law exponent that is lower by one, therefore the Hertzian fit does not provide reasonable data (Fig. 2B,C). Unlike in case of the spring element, the curves now depend on the indentation history and differ for the triangular and sinusoidal ramps. The case of a single dashpot element might correspond to the viscous flow or complete plastic deformation.

The combination of a spring and a dashpot in parallel, known as the Kelvin-Voight element, has the following relaxation function:

$$E(t) = E_\infty + \eta\delta_D(t); \tag{2}$$

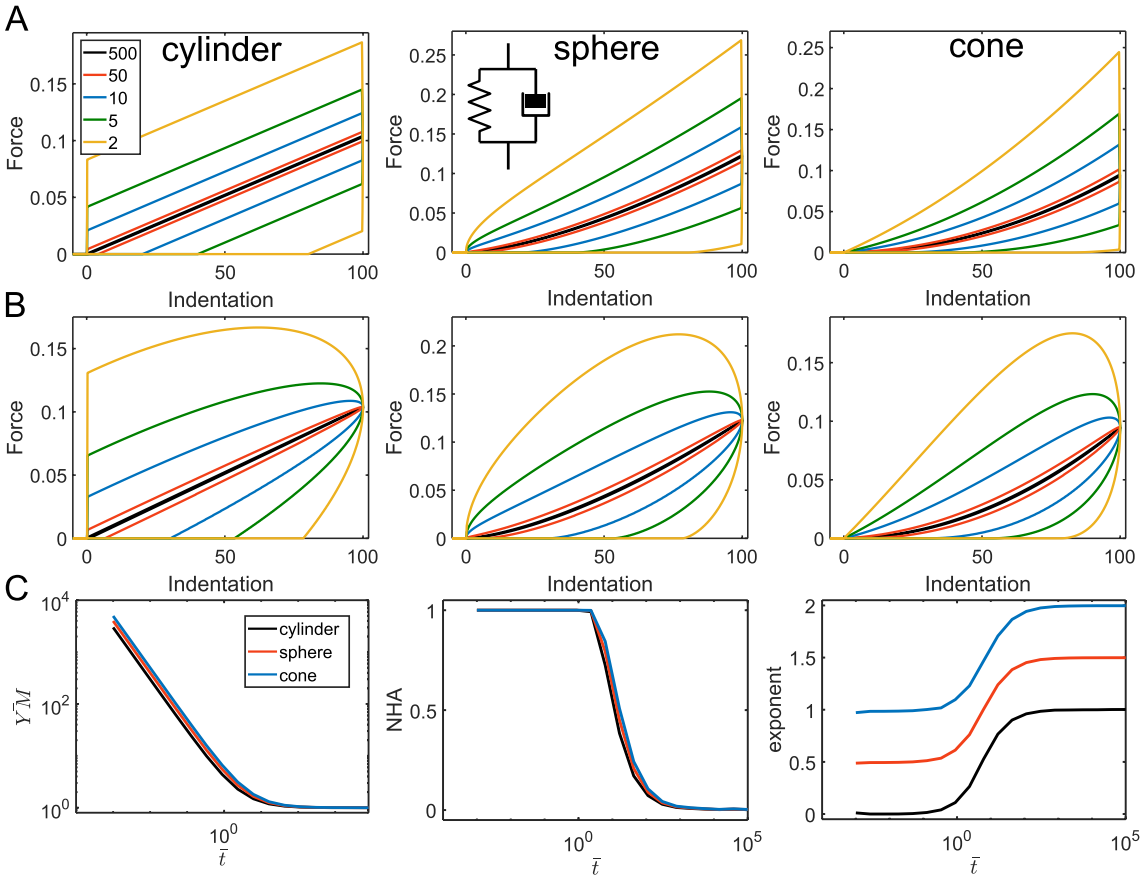

Figure 3. The force curves and parameters acquired from the force curves for the Kevin-Voight model. (**A**) The force curves for the triangular displacement; cylindrical, spherical, and conical indenters, and varied t_{ind}/τ_{KV} ratio (shown with different line colors), $E_\infty = 1{,}000$ Pa is fixed. (**B**) The force curves for the sinusoidal displacement. (**C**) Dependencies for the normalized YM (YM/E_∞), NHA, and curve exponent on the normalized indentation time $\bar{t} = t_{ind}/\tau_{KV}$.

where the subscript "∞" symbolizes a long-term response here and thereafter (E_∞ corresponds to the long-term modulus). The characteristic time of the model is $\tau_{KV} = \frac{\eta}{E_{inf}}$. At short indentation times ($t_{ind} << \tau_{KV}$), the behavior is dominated by the dashpot, and at long indentation times ($t_{ind} >> \tau_{KV}$)—by the spring (the spring modulus corresponds to E_∞). Accordingly, the NHA decreases with the indentation time, it is close to zero at slow rates, and close to one at fast rates (Fig. 3). The effective YM is proportional to the indentation rate at short times, but then it reaches a plateau corresponding to E_∞ at long times. The curve exponent at long times is equal to the Hertzian one, but as for the single.

dashpot model, it is lower by one at short times. In the actual experiments, such a huge deviation from the Hertzian exponent could indeed be observed when the dissipation (NHA) is large, for example in AFM experiments on cells at very high indentation rates[27] (Fig. S3). A notable feature of the model is the jump in the force (discontinuity) at the initial contact for the case of the cylindrical indenter, that is caused by the dashpot and could be seen in FEM simulations as well[28] (Fig. S1). Another discontinuity is the drop of the force at the turning point of the triangular displacement caused by the dashpot element (Fig. 3A). The Kelvin-Voight element can describe the plastic flow of the material during the indentation. In the normalized coordinates $\bar{F}$ versus $\bar{\delta}$, the curve shape is determined solely by the t_{ind}/τ_{KV} ratio. The curves of NHA, YM, and exponent versus normalized contact time only weakly depend on the probe geometry (Fig. 3C). The data for the sinusoidal ramp demonstrated similar trends and are not shown here.

For another combination, a spring and a dashpot in series, known as the Maxwell element, the relaxation function presents a well-known exponential decay:

$$E(t) = E_0 e^{-\frac{t}{\tau}}; \tag{3}$$

where the subscript "0" symbolizes the instantaneous response here and thereafter (spring modulus corresponds to the instantaneous modulus E_0). The characteristic time $\tau_{MW} = \frac{\eta}{E_0}$. At short indentation times $t_{ind} << \tau_{MW}$ the behavior is dominated by the spring, and at long indentation times $t_{ind} >> \tau_{MW}$—by the dashpot. Accordingly, the NHA increases with the indentation time, it is close to zero at fast rates, and close to one at slow rates, which is opposite to the Kelvin-Voight model. The effective YM is proportional to the indentation rate at long times, but a plateau corresponding to E_0 is observed at short indentation times. The curve exponent at short

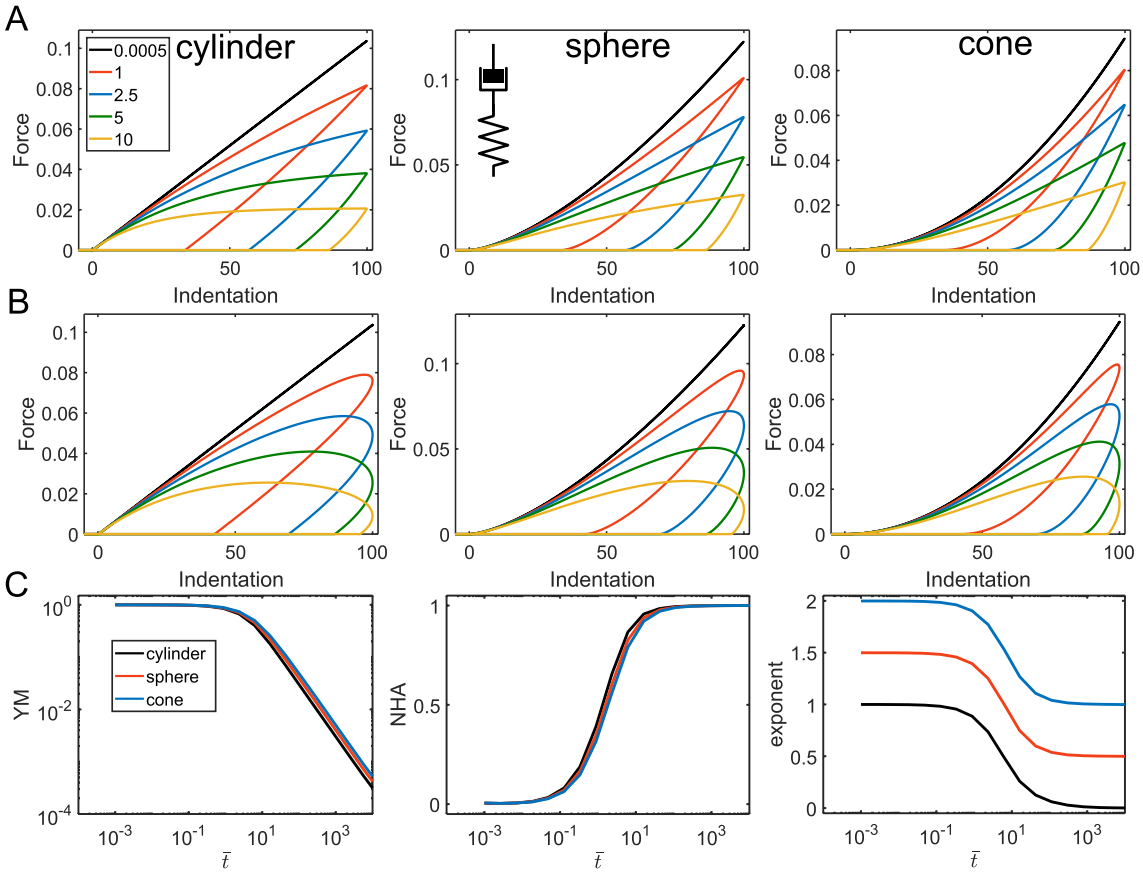

Figure 4. The force curves and parameters acquired from the force curves for the Maxwell model. (**A**) The force curves for the triangular displacement; cylindrical, spherical, and conical indenters, and varied t_{ind}/τ_{MW} ratio (shown with different line colors), $E_0 = 1{,}000$ Pa is fixed. (**B**) The force curves for the sinusoidal displacement. (**C**) Dependencies for the normalized YM (YM/E_0), NHA, and curve exponent on the normalized indentation time $\bar{t} = t_{ind}/\tau_{MW}$.

times is equal to the Hertzian one and is lower by one at long times. Again, the probe geometry and ramp type only weakly affect the observed dependencies (Fig. 4).

The standard linear solid model (Zener model) can be represented as the Maxwell element in parallel with a second spring (E_{s2}) that determines the long-term modulus of the system. The short-term modulus is a combination of the moduli of the two springs $E_0 = E_{s1} + E_{s2}$. The relaxation function is:

$$E(t) = E_{s1}e^{-\frac{t}{\tau}} + E_{s2} = (E_0 - E_\infty)e^{-\frac{t}{\tau}} + E_\infty; \quad (4)$$

which differs from the relaxation function of the Maxwell element by the presence of the E_∞ term. The model has the characteristic times $\tau_{rel} = \frac{\eta}{(E_0 - E_\infty)}$ and $\tau_{creep} = \frac{E_0\eta}{E_\infty(E_0 - E_\infty)}$, known to be characteristic times of relaxation and creep, respectively. From here, for the larger E_0/E_∞ ratio and the same τ_{rel} value, the relaxation will be more pronounced and will take more time. At short and long indentation times, there are plateaus for all dependencies, with the moduli corresponding to E_0 and E_∞, respectively, the curve exponent corresponding to the Hertzian one, and NHA close to zero. The maximum.

NHA is observed at values slightly larger than τ_{rel} and τ_{creep}; the larger E_0/E_∞ ratio provides a larger and wider negative peak. At the very large E_0/E_∞ ratios, the model behaves as a single dashpot in this intermittent regime, while at small ratios the viscoelastic behavior will be unnoticeable. The curve exponent is affected in a similar way (Fig. 5A–C).

The SLS model could be seen as a particular case of the generalized Maxwell model, where several Maxwell elements are connected in parallel. We analyzed a case with two such elements and a spring:

$$E(t) = E_{s1}e^{-\frac{t}{\tau_1}} + E_{s2}e^{-\frac{t}{\tau_2}} + E_{s3}; \quad (5)$$

where $E_0 = E_{s1} + E_{s2} + E_{s3}$, $E_{\inf} = E_{s3}$. The main outcome of such a model is that, locally, near the relaxation time of one of the Maxwell elements, the shape of the force curves will be determined by this particular element. If the relaxation times of both Maxwell elements are close to each other, then larger and wider peak for the NHA and curve exponent will be observed instead of two separate peaks (Fig. 5D).

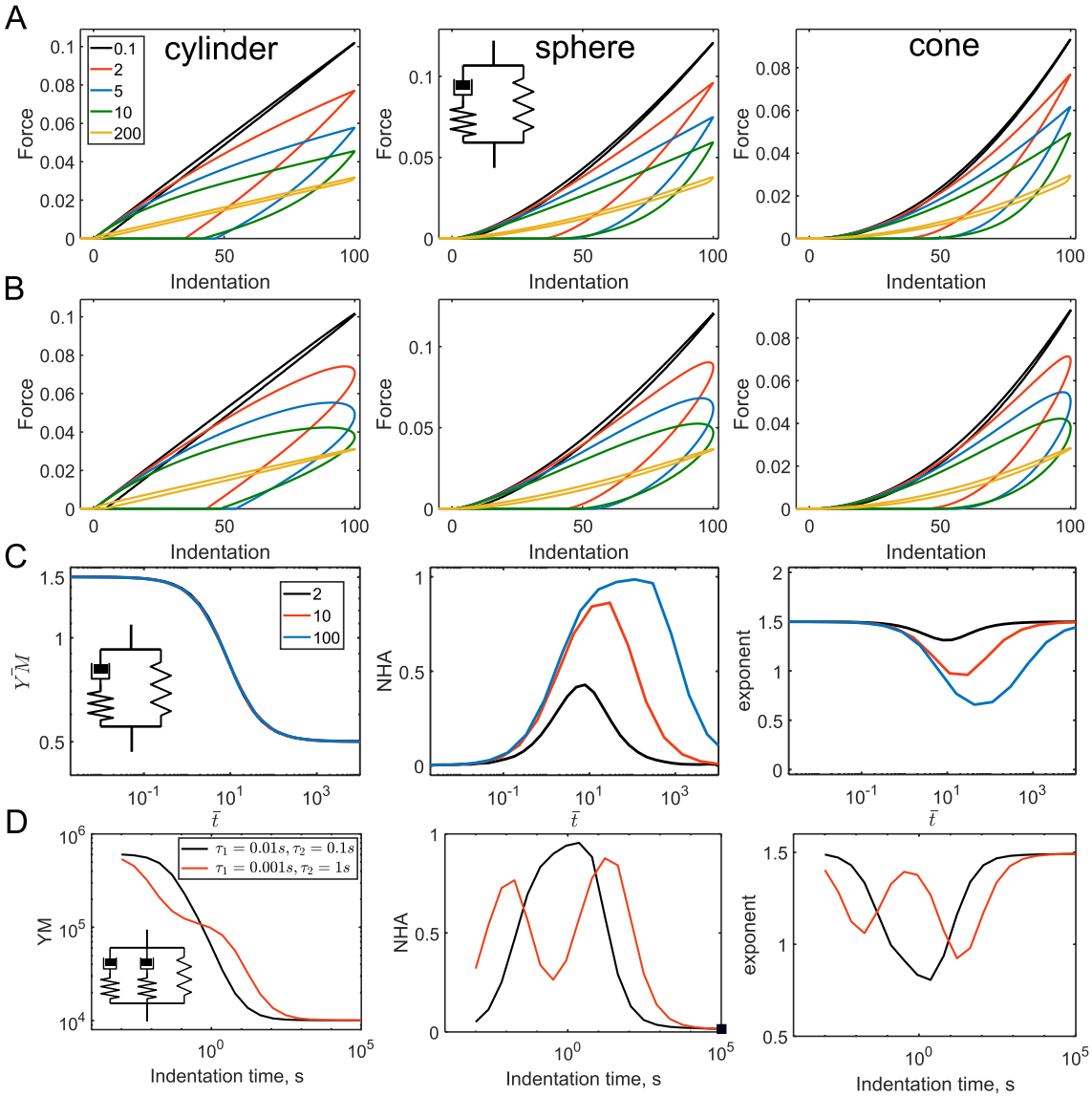

Figure 5. The force curves and parameters acquired from the force curves for the SLS model. (**A**) The force curves for the triangular displacement; cylindrical, spherical, and conical indenters, and varied t_{ind}/τ_{rel} ratio (shown with different line colors), $E_0 = 1{,}000$ Pa, $E_\infty = 300$ Pa are fixed. (**B**) The force curves for the sinusoidal displacement. (**C**) Dependencies for the normalized YM ($YM/(E_0 - E_\infty)$), NHA, and curve exponent on the normalized indentation time $\bar{t} = t_{ind}/\tau_{rel}$ for different E_0/E_∞ ratios. (**D**) Generalized Maxwell model with two relaxation times, two cases with a small and large difference in the relaxation times. $E_{s1} = 500$ kPa, $E_{s2} = 100$ kPa, $E_{s3} = 10$ kPa. Dependencies for the YM, NHA, and curve exponent on the indentation time. Here, absolute YM in Pa and time in seconds (s) are used for a better representation.

Fractional viscoelastic models. From the Fractional Calculus theory, another type of the basic viscoelastic element is a so-called springpot with a governing equation $\sigma(t) = K_\alpha d^\alpha \varepsilon(t)/dt^\alpha$. The element has two parameters, the unitless power-law exponent and the parameter K_α with units of [Pa s$^{-\alpha}$]. The Young's relaxation function can be written as:

$$E(t) = \frac{K_\alpha}{\Gamma(1-\alpha)} t^{-\alpha} = \frac{E_\alpha}{\Gamma(1-\alpha)} \left(\frac{t}{\tau}\right)^{-\alpha} = E_{\alpha 1} t^{-\alpha}; \quad (6)$$

where $\Gamma()$ is the Gamma function. It is worth stressing the meaning of the other parameters in the equation. The K_α parameter with units of [Pa s$^{-\alpha}$] is not very convenient and does not have a straightforward physical meaning. It is commonly replaced with $K_\alpha = E_\alpha \tau^\alpha$, where E_α is the Young modulus in [Pa] and τ is in [s]. However, these two parameters are not independent and are linked via K_α. To reduce the number of independent parameters back to two, we might assign $\tau = 1$ s, then the parameter $E_{\alpha 1} = E_{\alpha,\tau=1}/\Gamma(1-\alpha)$ will arise with units of [Pa] and a simple meaning of the value of the relaxation function at t = 1 s. However, for the correspondence of the

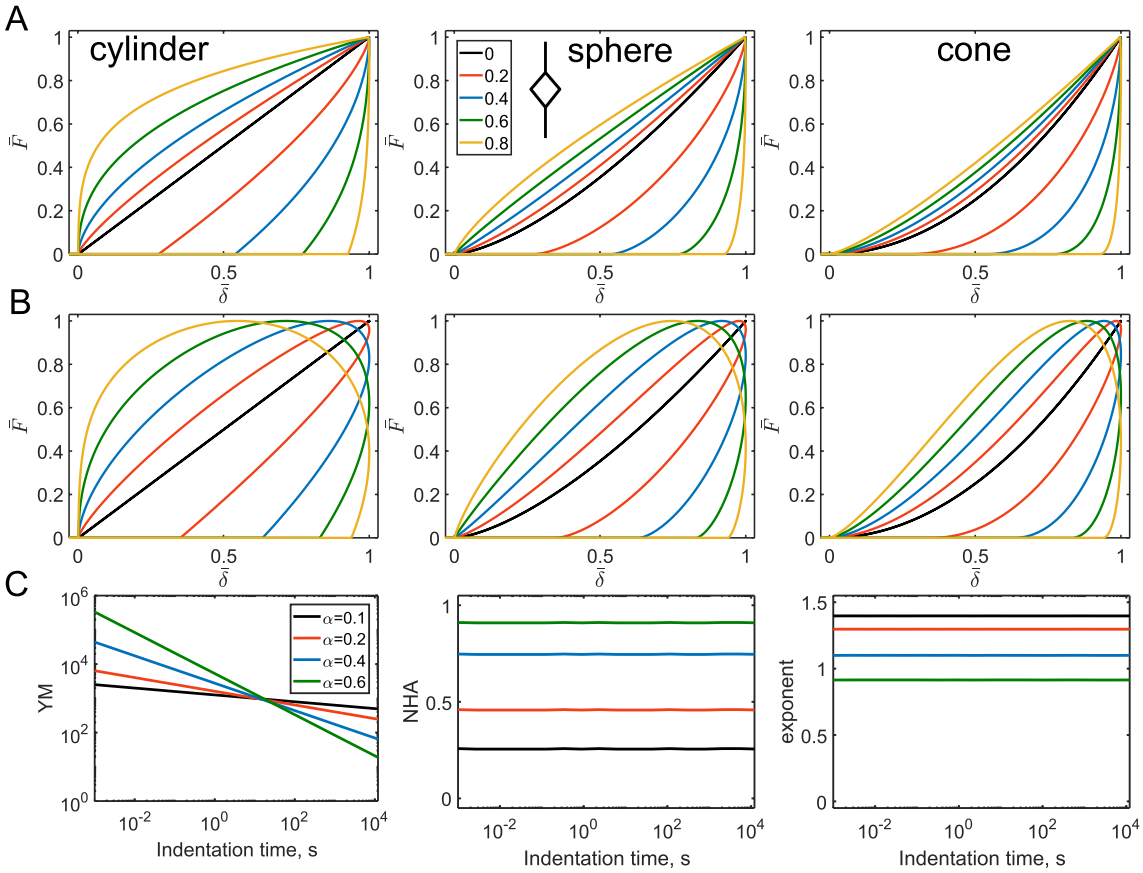

Figure 6. The force curves and parameters acquired from the force curves for the springpot model. (**A**) The force curves for the triangular displacement; cylindrical, spherical, and conical indenters, and varied α. (**B**) The force curves for the sinusoidal displacement. (**C**) Dependencies for the YM, NHA, and curve exponent on the indentation time, only for the spherical indenter, triangular displacement. Here, absolute YM in Pa and time in seconds (s) are used for a better representation, $E_{\alpha 1} = 1{,}000$ Pa is fixed.

units, the time in the last part of Eq. (12) should be considered as unitless ($t/[\tau = 1s]$). Notably, the model can be easily rescaled to any other characteristic time τ.

The springpot element intermediates between a spring and a dashpot through a fractional-order derivative α of the strain history ($0 < \alpha < 1$). The force curves constructed with the model demonstrate some interesting features: (1) In the normalized coordinates, the shape of the curve is defined solely by α (Fig. 6A,B); (2) The NHA and curve exponent parameters are independent of the indentation time and are also determined by α. The larger α value corresponds to the larger hysteresis. The curve exponent value approximately equals to its Hertzian value minus α; (3) Effective Young's modulus increases with the indentation rate following the power-law dependency with the same exponent α (Fig. 6C). These effects were similar for all the considered geometries, for the sinusoidal and triangular ramp loadings. Such behavior makes a simple guidance for the identification of the power-law behavior in experiments: the constant hysteresis in the force curves acquired at different rates, the power-law dependency of the effective modulus on the indentation rate. Such effects are indeed observed in experiments on cells in a wide range of indentation rates[5] (Fig. S4).

The springpot element could be used in various combinations with other elements, including other springpot elements. We will address some basic combinations here. A springpot in parallel with a spring will provide the following relaxation function:

$$E(t) = E_{\alpha 1} t^{-\alpha} + E_{\infty}; \tag{7}$$

where $E_{\infty} < E_{\alpha 1}$. This combination is also known as the fractional Kelvin-Voight model[29,30]. The difference with a single dashpot element is the presence of the long-term modulus at slow indentation rates. Therefore, the YM, curve exponent and NHA observe the gradual prolonged transition between the power-law and elastic regimes. The transition point is defined by the characteristic time $\tau = (E_{\alpha 1}/E_{\infty})^{\frac{1}{\alpha}}$ [s]; at shorter times, the behavior is dominated by the springpot. Thus, hysteresis increases with the indentation rate toward the certain limit defined by the α value (Fig. 7).

For a springpot and a spring in series, the resulted relaxation function is more complex due to the presence of the Mittag-Lefler function (ML) in the equation:

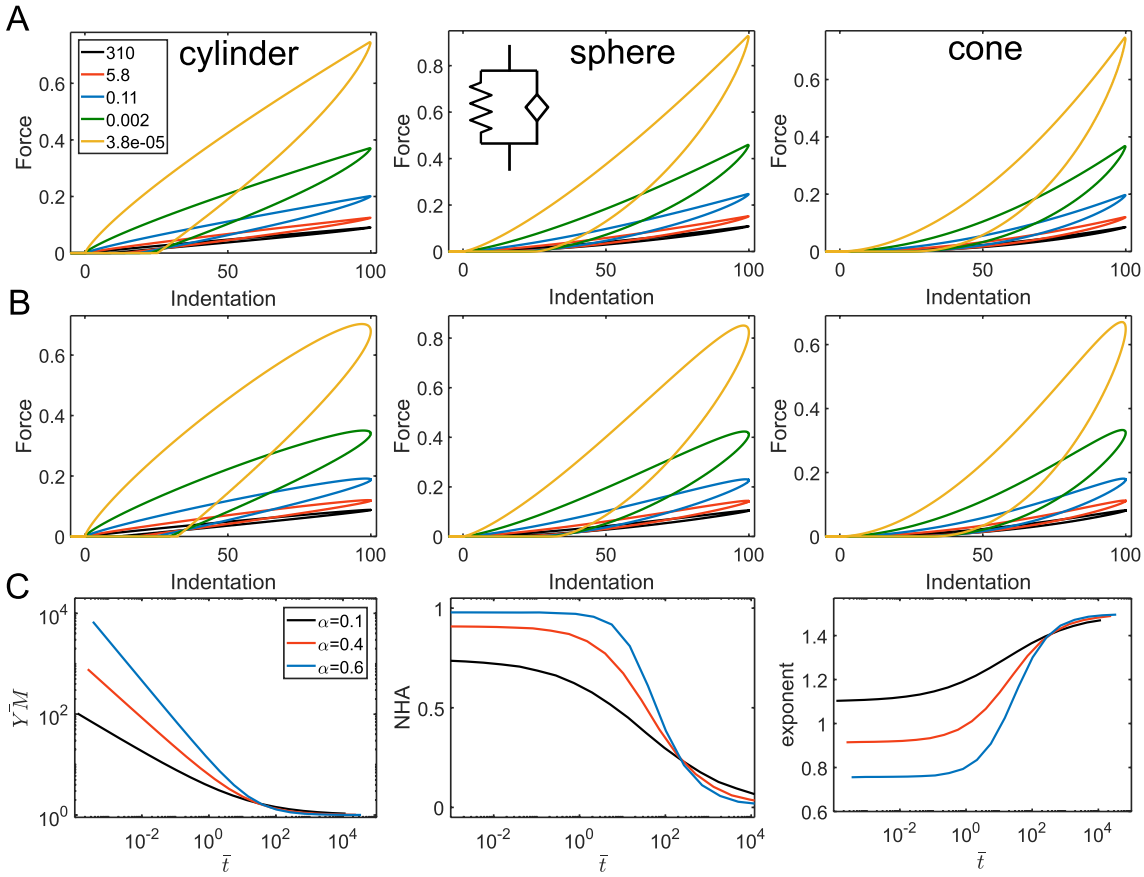

Figure 7. The force curves and parameters acquired from the force curves for the fractional Kelvin-Voight model. (**A**) The force curves for the triangular displacement; cylindrical, spherical, and conical indenters, $\alpha = 0.2$ and varied t_{ind}/τ ratio, $E_{\alpha 1} = 1{,}000$ Pa and $E_{\infty} = 600$ Pa. (**B**) The force curves for the sinusoidal displacement. (**C**) Dependencies for the normalized YM, NHA, and curve exponent on the normalized indentation time $\bar{t} = t_{ind}/\tau$ for different α values.

$$E(t) = E_0 ML_{\alpha}\left[-\frac{E_0}{E_{\alpha 1}}t^{\alpha}\right]. \tag{8}$$

The Mittag–Leffler function is a special function that arises from the solution of certain fractional differential equations and is calculated numerically. As opposed to the parallel combination, now the spring ($E_s = E_0$) dominate in response at short timescales and the springpot – at long timescales (Fig. 8). The characteristic transition time is $E_0/E_{\alpha 1}$ [s].

The same analogy could be observed in combinations of a springpot and a dashpot: when placed in parallel, the short-time response is controlled by the dashpot, and when in series—by the springpot. The relaxation functions are:

$$E(t) = E_{\alpha 1}t^{-\alpha} + \eta\delta_D(t); \tag{9}$$

$$E(t) = \eta^{\frac{\beta}{\beta-1}}\left(E_{\beta 1}\right)^{\frac{1}{1-\beta}}t^{-\beta}ML_{1-\beta,1-\beta}\left[-\frac{E_{\beta 1}}{\eta}t^{1-\beta}\right]; \tag{10}$$

for the parallel and serial arrangements, respectively (Fig. 9A,B). More generally, when a combination of two springpot elements is considered, the parallel arrangement leads to the short-time behavior controlled by the element with the higher exponent, and the long-time response—by the element with the lower exponent. The opposite is true when the elements are arranged in series. The relaxation functions for two springpot elements are as follows:

$$E(t) = E_{\alpha 1}t^{-\alpha} + E_{\beta 1}t^{-\beta}; \tag{11}$$

for the parallel arrangement; and for the serial arrangement:

$$E(t) = (E_{\alpha 1})^{\frac{\beta}{\beta-\alpha}}\left(E_{\beta 1}\right)^{\frac{\alpha}{\alpha-\beta}}t^{-\beta}ML_{\alpha-\beta,1-\beta}\left[-\frac{E_{\beta 1}}{E_{\alpha 1}}t^{\alpha-\beta}\right]; \tag{12}$$

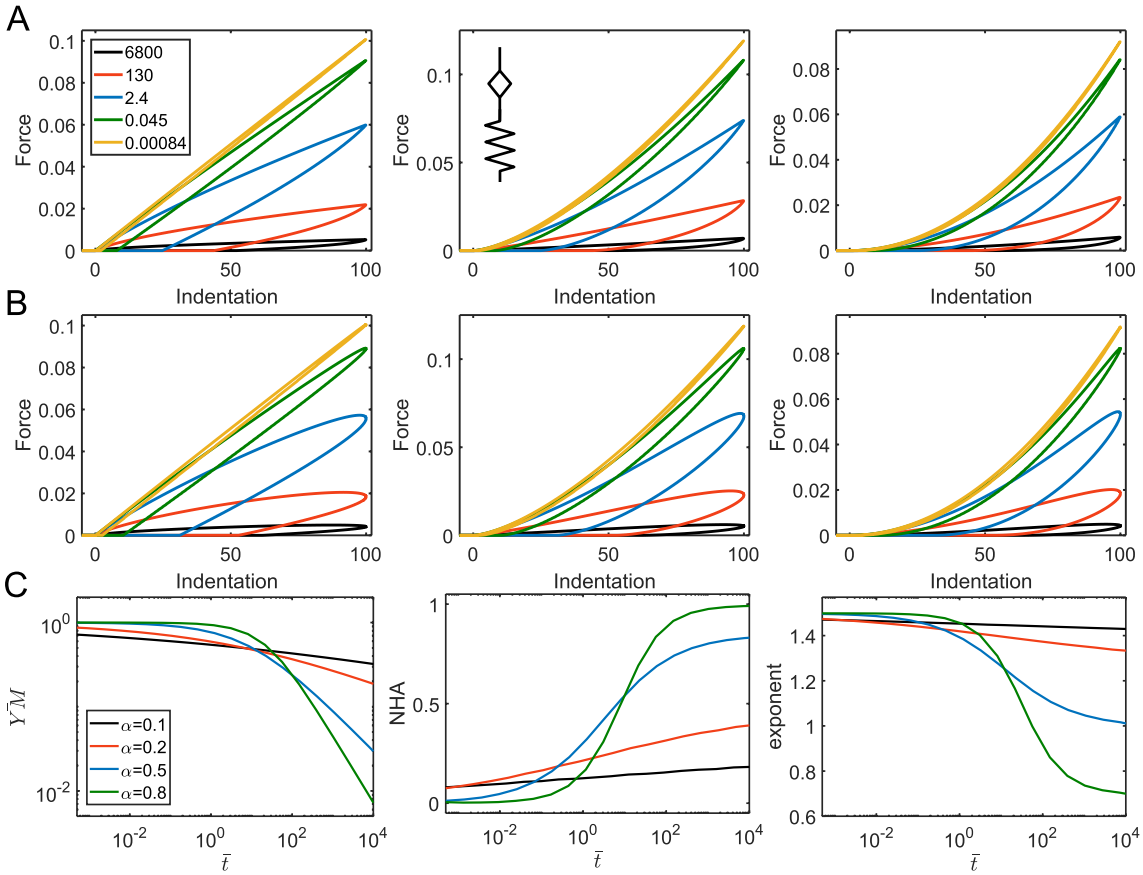

Figure 8. The force curves and parameters acquired from the force curves for the model representing by a springpot and a spring in series. (**A**) The force curves for the triangular displacement; cylindrical, spherical, and conical indenters, $\alpha = 0.4$ and varied t_{ind}/τ ratio, $E_0 = 1{,}000$ Pa. (**B**) The force curves for the sinusoidal displacement. (**C**) Dependencies for the normalized YM, NHA, and curve exponent on the normalized indentation time $\bar{t} = t_{ind}/\tau$ for different α values.

where $\alpha > \beta$ (Fig. 9C,D). All the previously considered models for serial arrangements of the elements could be seen as a particular case of the two serial springpot elements. When $\alpha = 1$, the springpot element reduces to the dashpot, and when $\beta = 0$, it reduces to the spring. The characteristic transition times, as was shown in[8], can be presented as $\tau_{parallel} = \left(\frac{E_{\alpha 1}}{E_{\beta 1}}\right)^{\frac{1}{\alpha-\beta}}$ and $\tau_{serial} = \left[(1-\alpha)\frac{E_{\alpha 1}}{E_{\beta 1}}\right]^{\frac{1}{\alpha-\beta}}$.

The addition of a spring in parallel to another element results in the addition of the long-term modulus E_∞ to the relaxation function. We will consider two such models here, the first one is a spring in parallel with a springpot and spring combination, also known as a fractional SLS (fractional Zener) model[31], with the following relaxation function:

$$E(t) = E_s ML_\alpha\left[-\frac{E_s}{E_{\alpha 1}}t^\alpha\right] + E_{\inf} = (E_0 - E_{\inf})ML_\alpha\left[-\left(\frac{t}{\tau_{fSLS}}\right)^\alpha\right] + E_{\inf}; \tag{13}$$

where $E_0 = E_s + E_{\inf}$ and the characteristic time is $\tau_{fSLS} = \left(\frac{E_{\alpha 1}}{E_s}\right)^{\frac{1}{\alpha}}$. As in the common SLS model, this model has plateau regions at short and long times corresponding to E_0 and $E_{\inf}$ elastic moduli. At $\alpha = 0$, the model reduces to the SLS model. Increase in α leads to the stretching of the transition region around the transition time, similar to the model known as the stretched exponent model[32]. Accordingly, the hysteresis in force curves is observed over a wider range of indentation times, while diminishing to zero at extremes (Fig. 10A).

The second model is a spring in parallel with a springpot and dashpot combination. The model was comprehensively studied in the recent works[8,33]. The relaxation function is:

$$E(t) = \eta^{\frac{\beta}{\beta-1}}\left(E_{\beta 1}\right)^{\frac{1}{1-\beta}} t^{-\beta} ML_{1-\beta,1-\beta}\left[-\frac{E_{\beta 1}}{\eta}t^{1-\beta}\right] + E_{\inf}. \tag{14}$$

The behavior of the model, as expected, is similar to the springpot—dashpot combination with a transition to the elastic regime at the long timescales. On the other hand, the model reduces to the SLS model when $\beta = 0$. The largest hysteresis in force curves is observed in the middle region where the dashpot is active, then, at short timescales, the hysteresis reduces toward the values defined by the springpot exponent β (Fig. 10B).

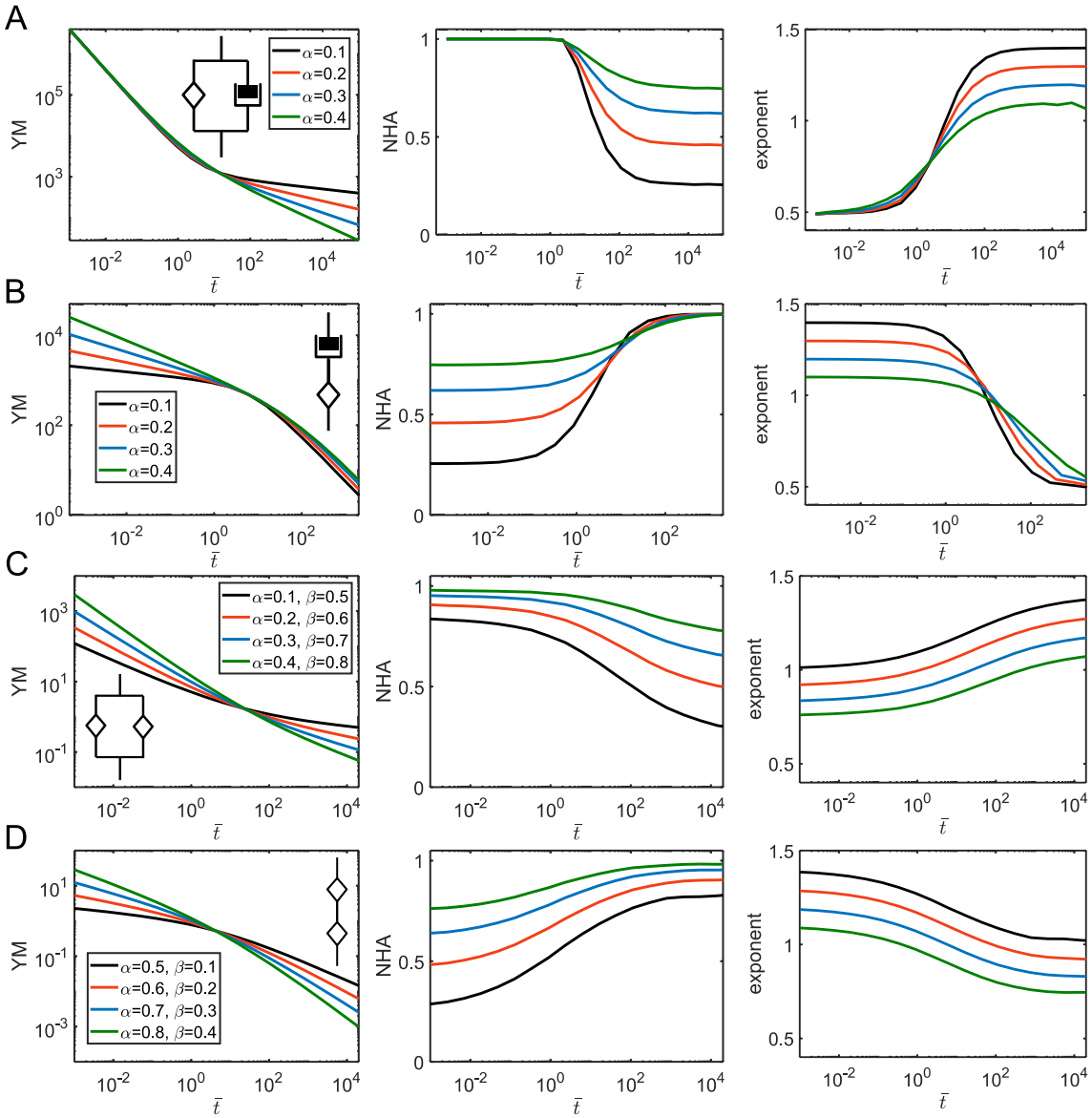

Figure 9. The parameters acquired from the force curves for a springpot and a dashpot in different combinations. Dependencies for the YM, NHA, and curve exponent on the normalized indentation time $\bar{t} = t_{ind}/\tau$, where τ is the characteristic time of the corresponding model, for different α (and β) values for a springpot in parallel with a dashpot (**A**); a springpot in series with a dashpot (**B**); a springpot in parallel with another springpot; (**D**) a springpot in series with another springpot. $E_{\alpha 1} = 1{,}000$ Pa and $\eta = 1{,}000$ Pa s (**A**); $E_{\beta 1} = 1{,}000$ Pa and $\eta = 10^4$ Pa s (**B**); $E_{\alpha 1} = 1$ Pa and $E_{\beta 1} = 1$ Pa (**C**); $E_{\alpha 1} = 1$ Pa and $E_{\beta 1} = 1$ Pa (**D**).

General dependencies of the curve parameters on the relaxation function. Some general dependencies could be drawn from the provided numerical analysis. Importantly, the shape of the force curves is strongly affected by the relaxation function of the material. A huge deviation from the Hertzian curve exponent (up to minus one) is possible when relaxation is significant. It correlates with the large hysteresis, NHA, of the curve. Since the elastic assumption is often used to fit the force curves, the lower curve caused by viscoelasticity might be misinterpreted as non-linear elasticity (strain-softening), since the fit of shallower regions will provide a higher YM and the fit of the deeper regions—a lower YM. Otherwise, if the real non-linearity like strain-stiffening is presented, viscoelasticity might conceal it to some extent.

The dependencies of the apparent YM, NHA, and curve exponent versus indentation time were close for the studied indenter geometries and indentation histories. By comparison with the actual relaxation functions, we have found that the apparent YM corresponds very closely to the time-averaged value of the relaxation function with the limits from $t = 0$ to $t = t_{ind}/4$ (Fig. 11A):

$$< E >= \frac{1}{t_{ind}/4} \int_0^{t_{ind}/4} E(t)dt. \tag{15}$$

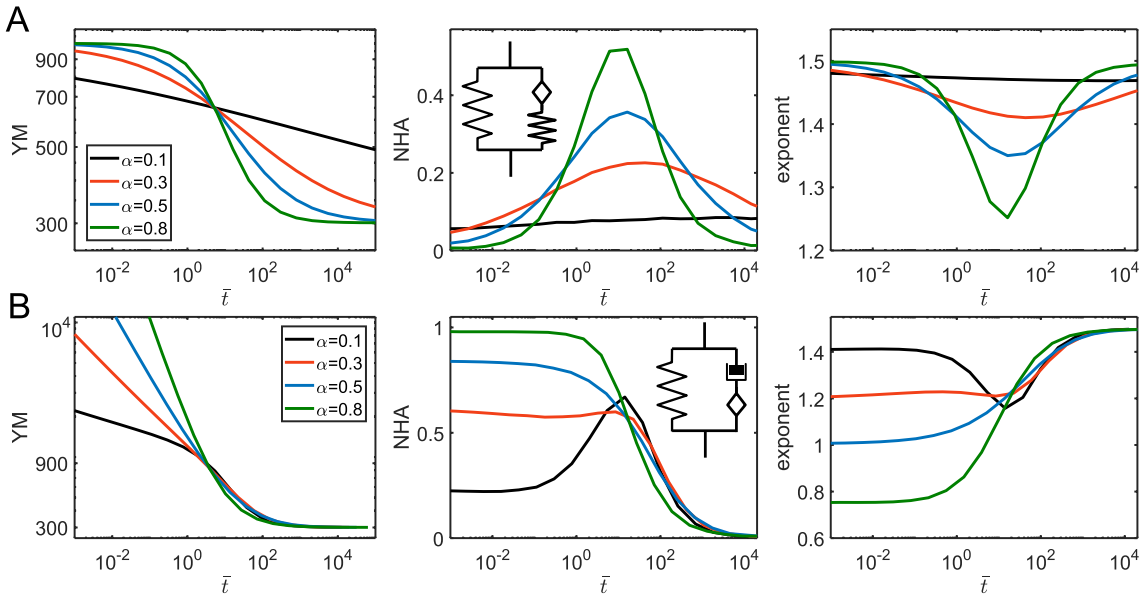

Figure 10. The parameters acquired from the force curves for the two three-element fractional viscoelastic models: a spring in parallel with a springpot and spring combination (**A**), a spring in parallel with a springpot and dashpot combination (**B**). Dependencies for the YM, NHA, and curve exponent on normalized indentation time $\bar{t} = t_{ind}/\tau$, where τ is the characteristic time of the corresponding model, for different α values. $E_0 =$ 1,000 Pa, $E_\infty = 300$ Pa (**A**); $E_{\beta 1} = 1{,}000$ Pa, $E_\infty = 300$ Pa (**B**).

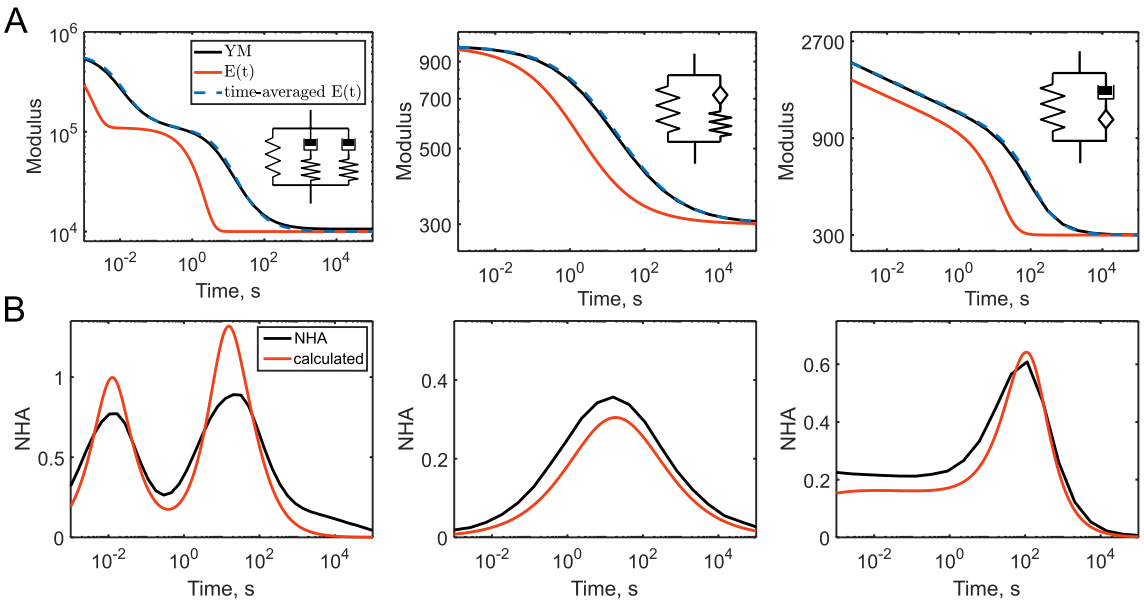

Figure 11. Comparison of the apparent YM (**A**) and NHA (**B**) acquired from the force curves with the relaxation function for the three viscoelastic models: Generalized Maxwell model with two relaxation times; a spring in parallel with a springpot and spring combination; a spring in parallel with a springpot and dashpot combination. (**A**) The YM, the relaxation function *E(t)*, and the time-averaged relaxation function. (**B**) The NHA and slope of the time-averaged relaxation function on the logarithmic scale.

The upper limit corresponds to half of the approach time since only the approach curve data are used for the YM calculation. The dependencies of the NHA and curve exponent values are more complex. As a first approximation, they are related to the local slope of the relaxation function on a logarithmic scale. Indeed, we have found that the doubled slope of the time-averaged relaxation function, shown in Fig. 11A, is close to the observed NHA values (Fig. 11B). A zero slope corresponds to the elastic regions with a zero NHA and Hertzian exponent value; and the maximum slope, which is equal to one (for the dashpot), leads to the NHA = 1 and a decrease in the exponent by one. It should also be noted, that NHA is a fraction of the energy dissipated during

the indentation cycle, and thus it is related to the loss tangent (ratio of the loss modulus to the storage modulus) at the frequency corresponding to $1/t_{ind}$. As suggested previously[17,27], the equations for the time-to-frequency-domain conversion[9] can be used for the assessment of the complex Young's modulus at this apparent frequency.

Discussion

The shape of the force-indentation curves is well-predicted by the underlying viscoelastic relaxation function; the analytical, numerical, and simulation solutions provide well-matched results. Viscoelasticity causes substantial deviation of the curve shape from the purely elastic response. The curve exponent decreases from the Hertzian value, which might be misinterpreted as strain-softening if the elastic assumption is used. The presence of the hysteresis area is a clear sign of the viscoelastic response (in the absence of strong adhesion and plasticity).

Several approaches might be used to extract the information about the relaxation function from the indentation data. One of simple ways is to observe the dependencies of the apparent YM and NHA on the indentation rate and to compare them with the predictions from the relaxation functions. For example, the presence of the constant NHA over the wide range of times is an indicator of the power-law rheology. The idea of using the YM versus indentation rate was implemented in the previous studies[34,35]. In the case of the power-law rheology, the power-law exponent might be extracted from such a dependency. The empirical comparison shows that the apparent modulus does not follow the relaxation function exactly, but it is very close to the time-averaged value of this function (Fig. 11A). The NHA is related to the local slope of the relaxation function on a logarithmic scale. A large hysteresis in the curve correlates with the strong dependency of the YM on the indentation rate.

More advanced approaches involve algorithms for the fitting of the force curves to the preselected viscoelastic models[5,16,17] or algorithms for the direct reconstruction of the relaxation function. In both cases, however, it is useful to obtain experimental curves in a wide range of indentation rates, and thus, it is useful to know how the curves should look for different viscoelastic models. This work might also be a basis for the further development of the more advanced models involving convolution of the viscoelasticity with the sample non-linearity, adhesion, anisotropy and other effects.

Methods

Linear viscoelasticity theory for indentation experiments. We will base the further description on the solution of the indentation problem of a viscoelastic half-space provided by Ting[24,25]. The solution was obtained for the cases of an arbitrary varying radius of the contact area, while here we will concentrate our attention on the load history with a single maximum: the contact area increases first during the approach phase (indenter is pressed into the sample) and then decreases during the retraction phase of the displacement-controlled experiment. The solution for the approach curve coincide with the solution provided by Lee and Radok[21], while the solution for the retraction curve requires an auxiliary function $t_1(t)$. The $t_1(t)$ auxiliary function was introduced as a time point t_1 during the approach phase which corresponds to the same contact area at a time point t during the retraction phase. The Lee-Radok's and Ting's solutions match for both the approach and retraction curves for a cylindrical indenter and used indentation histories due to the constant contact area. The solution also assumes that a rigid indenter is smooth and axisymmetric but otherwise might have an arbitrary shape. Here we will consider the three most widely used indenter geometries (Fig. 1A): cylinder, sphere, and cone (or pyramid, the difference will be only in the geometrical factor). For the indentation displacement-controlled experiment, the Ting's solution could be presented in the following form[5]:

$$F_{appr}(t,\delta(t)) = C_{geom}\int_0^t E(t-\xi)\frac{\partial \delta^n}{\partial \xi} f_{BEC}(\delta)d\xi, \quad \dot{a} >= 0, \;\; 0 \le t \le t_m; \tag{16}$$

$$F_{retr}(t,\delta(t)) = C_{geom}\int_0^{t_1(t)} E(t-\xi)\frac{\partial \delta^n}{\partial \xi} f_{BEC}(\delta)d\xi, \quad \dot{a} < 0, \;\; t \ge t_m \ge t_{ind}; \tag{17}$$

$$\int_{t_1(t)}^t E(t-\xi)\frac{\partial \delta}{\partial \xi}d\xi = 0; \tag{18}$$

where F is the force acting on the cantilever during the approach (F_{appr}) or the retraction (F_{retr}); δ is the indentation depth; a is the contact area; $t_1(t)$ function is determined by the Eq. (18); t is the indentation time initiated at initial contact (t_m is the time when the maximum contact radius is reached, t_{ind} is the duration of a complete indentation cycle); ξ is the dummy time variable required for the integration; $E(t)$ is the relaxation function (Young's relaxation modulus); n and C_{geom} are constants related to the indenter shape[20], e.g.: $n = 1, C_{cyl} = 2R_{yl}/(1-\nu^2)$ for a cylindrical punch (R_{cyl} is the radius of the cylinder); $n = 2, C_{cone} = 2(tan\alpha_{cone})/\pi/(1-\nu^2)$ for a conical indenter (α_{cone} is the included half-angle of the cone); $n = 3/2, C_{sphere} = 4\sqrt{R}/3/(1-\nu^2)$ for a paraboloid/spherical indenter ($R >> \delta$ is the radius of the sphere); ν is the Poisson's ratio of the sample (assumed to be time-independent). $f_{BEC}(\delta)$ is the tip geometry dependent correction coefficient for the finite thickness of the sample attached to the hard substrate[28,36]. This factor does not depend on time and could be neglected when the sample thickness is much larger than the tip-sample contact area. Equation (16) for F_{appr} (Lee-Radok's solution) can also be used to describe the force during the retraction phase, but with limited accuracy. The Ting's solution requires calculation of $t_1(t)$ for the retraction phase. As can be seen from Eq. (18), the $t_1(t)$ function is common for all the indenter geometries but depends on the indentation history and the viscoelastic model.

The Young's relaxation modulus $E(t)$ is a function which determines the viscoelastic behavior of the material and is defined by a specific constitutive viscoelastic model. It is related to the shear stress relaxation modulus as

$G(t) = E(t)/2/(1+\nu)$[37]. Note, that the time-independent Poisson's ratio is assumed here. A "reduced" form of the relaxation (creep) function can be obtained that represents the function normalized by its value at a certain time point, usually, $t = 0$ or $t = \infty$. However, such an approach does not always work since some relaxation functions have infinite or zero values at these time points.

Most modern indenters offer both load and displacement control indentation testing. For example, in a typical AFM experiment, the load is applied by expanding the piezo. The system controls the rate of expansion/retraction of the piezo, but neither force nor indentation histories are controlled directly. The indentation depth δ is related to the piezo displacement Z as:

$$\delta(t) = z(t) - z_0 - d; \tag{19}$$

where z_0 is the contact point position (position of the undisturbed sample surface) and d is the cantilever deflection. The simplified relation might be considered if the cantilever (or another force sensor) is quite stiff and its deflection is much lower than the indentation depth. If we also place the zero of the displacement axis at the contact point position ($z_0 = 0$), the simplified indentation function will be: $\delta(t) = z(t)$. From here, it is possible to obtain analytical solutions for certain relaxation functions and indentation histories, and this simplification was used in this work.

Here, we will consider two indentation histories, a triangular linear ramp (ramp) and sinusoidal (sin) probe movement (Fig. 1B):

$$\delta_{ramp}(t) = \begin{cases} \nu t, & 0 \le t \le t_m \\ \nu(2t_m - t), & t > t_m \end{cases}; \tag{20}$$

$$\delta_{\sin}(t) = A\sin(\omega t). \tag{21}$$

For a triangular linear ramp, the maximum contact radius is reached at $t = t_m$ and then it decreases during retraction, the maximum indentation depth is $\delta_m = \nu t_m$. For the sinusoidal displacement, the maximum contact radius is reached at $t_m = \frac{\pi}{2\omega}$ corresponding to a quarter period of the sin wave, the amplitude A is set equal to δ_m. The t_m value is related to the total probe-sample contact time (indentation time, t_{ind}) as $t_m < t_{ind} < 2t_m$, since the contact area is always present during the approach phase, but would vanish at some point during the retraction phase. The sinusoidal ramp could be beneficial at high indentation rates, since, unlike the triangular ramp, it does not produce an abrupt change in the indentation speed around the turning point. The sinusoidal ramp is used, for example, in the Peak-Force Tapping technique[38] that allows acquisition of force maps with a high speed in AFM experiments.

Numerical and analytical solutions of the Ting's model. The MATLAB code based on the previous works[5,27] was used here to obtain a numerical solution of the Ting's model. It calculates the force versus time and the force versus displacement dependencies via numerical differentiation and integration steps, both for the approach and retraction parts of a force curve, the latter involves the numerical calculation of the $t_1(t)$ function by an iterative procedure. Arbitrary relaxation functions (in the form of the Young's relaxation modulus) and indentation histories (currently, with a single maximum in the contact radius versus time data) might be used as an input.

The analytical solutions were obtained for specific viscoelastic models as described in Appendix A. The Python version of the code for the numerical simulation of indentation curves is available at https://github.com/yu-efremov/ViscoIndent.

Finite element analysis. The finite element method (FEM) analysis was performed using the Abaqus CAE software (version 14, Simulia Corp., Providence, RI). The axisymmetric system was created with a cylindrical sample, having a radius of 100 μm and a height of 40 μm. The probe was modeled as a rigid body with the geometries of a flat-ended cylinder (radius of 0.4 μm), sphere (radius of 5 μm), or cone (half-angle of 85°). The sample mesh was optimized for each indenter geometry for a balance between the computational time and accuracy. The probe displacement was assigned for triangular and sinusoidal ramps. The viscoelastic behavior of samples was assigned via the Prony series coefficients. For the power-law rheology model, the relaxation function was approximated as the Prony series expansion including six terms, the coefficients were fitted in MATLAB.

Data availability

The datasets analyzed during the current study are available from the corresponding author on request and could be generated using the open-source Python code available at https://github.com/yu-efremov/ViscoIndent.

Received: 5 June 2020; Accepted: 23 July 2020
Published online: 06 August 2020

References

1. Qian, L. & Zhao, H. Nanoindentation of soft biological materials. *Micromachines.* **9**, 654. https://doi.org/10.3390/mi9120654 (2018).
2. Ebenstein, D. M. & Pruitt, L. A. Nanoindentation of biological materials. *Nano Today.* **1**, 26–33. https://doi.org/10.1016/S1748-0132(06)70077-9 (2006).
3. Efremov, Y. M., Okajima, T. & Raman, A. Measuring viscoelasticity of soft biological samples using atomic force microscopy. *Soft Matter* **16**, 64–81. https://doi.org/10.1039/C9SM01020C (2020).
4. Rother, J., Nöding, H., Mey, I. & Janshoff, A. Atomic force microscopy-based microrheology reveals significant differences in the viscoelastic response between malign and benign cell lines. *Open Biol.* **4**, 140046. https://doi.org/10.1098/rsob.140046 (2014).

5. Efremov, Y. M., Wang, W.-H., Hardy, S. D., Geahlen, R. L. & Raman, A. Measuring nanoscale viscoelastic parameters of cells directly from AFM force-displacement curves. *Sci. Rep.* **7**, 1541. https://doi.org/10.1038/s41598-017-01784-3 (2017).
6. Schierbaum, N., Rheinlaender, J. & Schäffer, T. E. Combined atomic force microscopy (AFM) and traction force microscopy (TFM) reveals a correlation between viscoelastic material properties and contractile prestress of living cells. *Soft Matter* **15**, 1721–1729. https://doi.org/10.1039/C8SM01585F (2019).
7. Rianna, C. & Radmacher, M. Comparison of viscoelastic properties of cancer and normal thyroid cells on different stiffness substrates. *Eur. Biophys. J.* **46**, 309–324. https://doi.org/10.1007/s00249-016-1168-4 (2017).
8. A. Bonfanti, J.L. Kaplan, G. Charras, A.J. Kabla, Fractional viscoelastic models for power-law materials, (2020) 1–28. https://arxiv.org/abs/2003.07834.
9. R. Lakes, Viscoelastic materials (Cambridge University Press, Cambridge, 2009) https://doi.org/10.1017/CBO9780511626722.
10. Magin, R. L. Fractional calculus in bioengineering, part 2. *Crit. Rev. Biomed. Eng.* **32**, 105–194. https://doi.org/10.1615/CritRevBiomedEng.v32.i2.10 (2004).
11. Efremov, Y. M., Cartagena-Rivera, A. X., Athamneh, A. I. M., Suter, D. M. & Raman, A. Mapping heterogeneity of cellular mechanics by multi-harmonic atomic force microscopy. *Nat. Protoc.* **13**, 2200–2216. https://doi.org/10.1038/s41596-018-0031-8 (2018).
12. Dokukin, M. & Sokolov, I. High-resolution high-speed dynamic mechanical spectroscopy of cells and other soft materials with the help of atomic force microscopy. *Sci. Rep.* **5**, 12630. https://doi.org/10.1038/srep12630 (2015).
13. Takahashi, R. & Okajima, T. Mapping power-law rheology of living cells using multi-frequency force modulation atomic force microscopy. *Appl. Phys. Lett.* **107**, 173702. https://doi.org/10.1063/1.4934874 (2015).
14. Cheng, Y. T. & Yang, F. Obtaining shear relaxation modulus and creep compliance of linear viscoelastic materials from instrumented indentation using axisymmetric indenters of power-law profiles. *J. Mater. Res.* **24**, 3013–3017. https://doi.org/10.1557/jmr.2009.0365 (2009).
15. Garcia, P. D., Guerrero, C. R. & Garcia, R. Nanorheology of living cells measured by AFM-based force-distance curves. *Nanoscale.* **12**, 9133–9143. https://doi.org/10.1039/c9nr10316c (2020).
16. Brückner, B. R., Nöding, H. & Janshoff, A. Viscoelastic properties of confluent MDCK II cells obtained from force cycle experiments. *Biophys. J.* **112**, 724–735. https://doi.org/10.1016/j.bpj.2016.12.032 (2017).
17. de Sousa, J. S. *et al.* Analytical model of atomic-force-microscopy force curves in viscoelastic materials exhibiting power law relaxation. *J. Appl. Phys.* **121**, 34901. https://doi.org/10.1063/1.4974043 (2017).
18. Ramesh Kumar, M. V. & Narasimhan, R. Analysis of spherical indentation of linear viscoelastic materials. *Curr. Sci.* **87**, 1088–1095 (2004).
19. Hertz, H. Über die Berührung Fester Elastischer Körper. *J. Für Die Reine u. Angew. Math.* **92**, 156–171 (1881).
20. Sneddon, I. N. The relation between load and penetration in the axisymmetric Boussinesq problem for a punch of arbitrary profile. *Int. J. Eng. Sci.* **3**, 47–57 (1965).
21. Lee, E. H. & Radok, J. R. M. The contact problem for viscoelastic bodies. *J. Appl. Mech.* **27**, 438–444 (1960).
22. Hunter, S. C. The Hertz problem for a rigid spherical indenter and a viscoelastic half-space. *J. Mech. Phys. Solids.* **8**, 219–234. https://doi.org/10.1016/0022-5096(60)90028-4 (1960).
23. Graham, G. A. C. The contact problem in the linear theory of viscoelasticity when the time dependent contact area has any number of maxima and minima. *Int. J. Eng. Sci.* **5**, 495–514. https://doi.org/10.1016/0020-7225(67)90037-7 (1967).
24. Ting, T. C. T. The contact stresses between a rigid indenter and a viscoelastic half-space. *J. Appl. Mech.* **33**, 845–854. https://doi.org/10.1115/1.3625192 (1966).
25. Ting, T. C. T. Contact problems in the linear theory of viscoelasticity. *J. Appl. Mech.* **35**, 248. https://doi.org/10.1115/1.3601188 (1968).
26. Garcia, P. D., Guerrero, C. R. & Garcia, R. Time-resolved nanomechanics of a single cell under the depolymerization of the cytoskeleton. *Nanoscale.* **9**, 12051–12059. https://doi.org/10.1039/C7NR03419A (2017).
27. Efremov, Y. M., Shpichka, A. I., Kotova, S. L. & Timashev, P. S. Viscoelastic mapping of cells based on fast force volume and PeakForce Tapping. *Soft Matter* **15**, 5455–5463. https://doi.org/10.1039/C9SM00711C (2019).
28. Garcia, P. D. & Garcia, R. Determination of the viscoelastic properties of a single cell cultured on a rigid support by force microscopy. *Nanoscale.* **10**, 19799–19809. https://doi.org/10.1039/C8NR05899G (2018).
29. Zhang, H., Wang, Y. & Insana, M. F. Ramp-hold relaxation solutions for the KVFD model applied to soft viscoelastic media. *Meas. Sci. Technol.* **27**, 25702. https://doi.org/10.1088/0957-0233/27/2/025702 (2016).
30. Zhang, H. *et al.* Modeling ramp-hold indentation measurements based on Kelvin-Voigt fractional derivative model. *Meas. Sci. Technol.* **29**, 035701. https://doi.org/10.1088/1361-6501/aa9daf (2018).
31. Carmichael, B., Babahosseini, H., Mahmoodi, S. N. & Agah, M. The fractional viscoelastic response of human breast tissue cells. *Phys. Biol.* **12**, 46001. https://doi.org/10.1088/1478-3975/12/4/046001 (2015).
32. Okajima, T. *et al.* Stress relaxation of HepG2 cells measured by atomic force microscopy. *Nanotechnology.* **18**, 084010. https://doi.org/10.1088/0957-4484/18/8/084010 (2007).
33. Bonfanti, A., Fouchard, J., Khalilgharibi, N., Charras, G. & Kabla, A. A unified rheological model for cells and cellularised materials. *R. Soc. Open Sci.* **7**, 190920. https://doi.org/10.1098/rsos.190920 (2020).
34. Caporizzo, M. A. *et al.* Strain-rate dependence of elastic modulus reveals silver nanoparticle induced cytotoxicity. *Nanobiomedicine.* **2**, 9. https://doi.org/10.5772/61328 (2015).
35. Efremov, Y. M. *et al.* The effects of confluency on cell mechanical properties. *J. Biomech.* **46**, 1081–1087. https://doi.org/10.1016/j.jbiomech.2013.01.022 (2013).
36. Garcia, P. D. & Garcia, R. Determination of the elastic moduli of a single cell cultured on a rigid support by force microscopy. *Biophys. J.* **114**, 2923–2932. https://doi.org/10.1016/j.bpj.2018.05.012 (2018).
37. Landau, L. D. & Lifshitz, E. M. *Theory of Elasticity* (Pergamon Press, Oxford, 1989).
38. Kaemmar, S. B. Introduction to Bruker's ScanAsyst and PeakForce Tapping AFM technology. *Appl. Note.* **133**, 12 (2011).

Acknowledgements

This study was supported by the Russian academic excellence project "5-100" (FEM simulations), by the Russian Science Foundation under the grant No. 19-79-00354 (Yu.M.E., development of numerical algorithms) and by the grant of the President of the Russian Federation for young scientists MK-1613.2020.7 (Yu.M.E., data analysis).

Author contributions

Yu.M.E. and P.S.T. designed the study. Yu.M.E. performed the computational analysis and prepared the figures. Yu.M.E. and S.L.K. wrote the main manuscript text. All authors discussed and reviewed the manuscript.

Competing interests

The authors declare no competing interests.

Additional information

Supplementary information is available for this paper at https://doi.org/10.1038/s41598-020-70361-y.

Correspondence and requests for materials should be addressed to Y.M.E.

Reprints and permissions information is available at www.nature.com/reprints.

Publisher's note Springer Nature remains neutral with regard to jurisdictional claims in published maps and institutional affiliations.